ECS Transactions, 41 (1) 1709-1717 (2011)
10.1149/1.3635702 ©The Electrochemical Society

Graphene-Enriched Co_9S_8-N-C Non-Precious Metal Catalyst for Oxygen Reduction in Alkaline Media

Gang Wu[a], Hoon T. Chung[a], Mark Nelson[a], Kateryna Artyushkova[b], Karen L. More[c], Christina M. Johnston[a], and Piotr Zelenay[a]

[a] Materials Physics and Applications Division, Los Alamos National Laboratory, Los Alamos, New Mexico 87545, USA
[b] Department of Chemical and Nuclear Engineering, University of New Mexico, Albuquerque, New Mexico 87131, USA
[c] Materials Science and Technology Division, Oak Ridge National Laboratory, Oak Ridge, Tennessee 37831, USA

In this work, a non-precious metal catalyst consisting of Co_9S_8 nanoparticles surrounded with nitrogen-doped graphene-like carbon (Co_9S_8-N-C) was developed for oxygen reduction in alkaline media. Improved activity has been measured with the Co_9S_8-N-C catalyst relative to Pt/C and a non-precious metal catalyst based on Fe instead of Co (Fe-N-C). An extensive physical characterization, including XRD, SEM, TEM, and XPS and electrochemical kinetic analysis was conducted to provide insight into the catalyst morphology and structure.

Introduction

In spite of a major progress achieved recently in the development of polymer electrolyte fuel cells (PEFCs), significant obstacles prevent PEFCS from entering the market ona large scale. One of the main such obstacles has been the dependence of fuel cells on platinum (Pt), an expensive and scarce resource. Although great effort has been devoted to exploring low-Pt and also non-precious metal catalysts for PEFCs (1-4), the durability of alternative catalysts in the strongly acidic environment of PEFCs is not yet sufficient. Poor kinetics of the oxygen reduction reaction (ORR) on cathodes in acid environments is another major hindrance on the way to the implementation of low-temperature fuel cells.

Alternatively, the use of alkaline media in fuel cell applications could offer several advantages over the acidic media, especially in terms of the electrocatalytic activity of alternative ORR catalysts and materials stability (5). According to the Nernst equation, the reaction potential shifts by -59 mV for every increase of 1 pH unit. As a result, the operating should shift by nominally -0.83 V when 1.0 mol/L H^+ solution of a strong acid is replaced with a 1.0 mol/L OH^- solution of a strong base. Such a potential shift can dramatically affect the local double-layer structure and the electric field at the electrode-electrolyte interface, leading to changes in the adsorption strength, even for neutral species (5). The decreased extent of spectator anion adsorption in alkaline media means that, in general, most electrocatalytic processes should become more favorable in alkaline solutions relative to those in acidic media (6). While the electrocatalytic advantages of using alkaline media are significant, the improved materials stability afforded by the use of alkaline electrolytes may be even more important. A wide variety of materials have exhibited comparable corrosion resistance in alkaline media to that of precious metals, a highly promising observation in the context of possible implementation of non-precious

catalysts in fuel cells (7). Water and ionic transport within the OH^--conducting electrolytes also benefit from a more favorable direction of the electro-osmotic drag, away from the cathode, which helps to prevent catalyst flooding, a major issue for PEFCs and direct methanol fuel cells (DMFCs) (8). This opposite direction of the electro-osmotic drag could also assist in the mitigation of methanol crossover, therefore offering an important advantage of the alkaline medium for DMFCs (9).

Continued development of alkaline polymer electrolyte fuel cells (APEFCs) to avoid the large performance losses resulted from precipitated K_2CO_3 has become an important subject of fuel cell research (10, 11). At the same time, non-precious metal catalysts have gradually become more attractive for APEFCs (5, 12). Recently, a promising ORR activity of Co-S and Co-Ni-S systems have been shown compared to transition-metal catalysts in 0.1 M KOH (13). It was reported that Co_3S_4 possess both high ORR activity and selectivity for a direct four-electron oxygen reduction to OH^- in 0.1 M KOH (14). Based on the adsorption bond strength of reactants, reaction intermediates formed, and products generated a (202) plane of Co_9S_8 was predicted to be active in O_2 (adsorption energies calculated with using the Vienna *ab-initio* simulation program, VASP) (15). In that modeling effort, S^{2-} was proposed for an adsorption site for O following the O–O bond scission.

In acidic media, nitrogen-doped graphitic carbon has been considered necessary for inducing an efficient multi-electron transfer in ORR catalysis. Nitrogen functionalities, pyridinic and quaternary nitrogen atoms in particular, have been tied to the ORR activity on the carbon surface (1, 16). This likely makes the nitrogen-doped carbon a suitable ORR active material to support Co-S particles in hybrid cathode catalysts.

In this work, a composite cathode catalyst was synthesized through a combination of catalytic properties derived from both Co-S species and nitrogen-doped carbon structure. This approach resulted in a notable improvement in oxygen reduction in alkaline media.

Experimental Details

Catalyst synthesis

Carbon support (Ketjenblack EC 300J) was first ultrasonically dispersed in 0.5 M HCl solution. The suspension was kept below 10°C while the aniline and the oxidant, ammonium peroxydisulfate in 0.5 M HCl, were added drop-wise. After stirring for 12 hours to allow aniline to fully polymerize, the transition metal salts, such as $Co(NO_3)_2 \cdot 6H_2O$ or $FeCl_3$, were added to the suspension to form complexes with the *in-situ* polymerized polyaniline. The suspension containing carbon, polymer and transition metal(s) was vacuum-dried using a rotary evaporator. The subsequent heat-treatment was performed at 900°C in an inert atmosphere of a nitrogen gas for 1 hour.

Physical characterization

The morphology and structure of the catalyst were characterized in Oak Ridge National Laboratory by scanning electron microscopy (SEM) on a Hitachi S-5400 instrument and by high-resolution transmission electron microscopy (HR-TEM) on a Hitachi HF3300 TEM operated at 300 kV. The crystallinity of various samples was determined by X-ray diffraction (XRD) using a Bruker AXS D8 Advance Diffractometer with Cu Kα radiation. The patterns were obtained at a scan rate of 5° min^{-1} with a step of 0.02°. X-ray photoelectron spectroscopy (XPS) was performed at the University of New Mexico on a Kratos Axis Ultra spectrometer using an Mg Kα X-ray source ($h\nu$=1253.6 eV), with emission voltage of 12 kV and emission current of 20 mA.

Electrochemical measurements

Rotating disc electrode (RDE) measurements of oxygen reduction were performed in a conventional three-electrode cell using a CHI Electrochemical Station (Model 750b) at room temperature (23 ± 2 °C). A graphite rod and an Ag/AgCl, (3.0 M NaCl, 0.209 V *vs.* SHE; 0.977 V *vs*. RHE) were used as the counter and the reference electrodes, respectively. ORR steady-state polarization curves were recorded in oxygen-saturated 0.1 M NaOH solution with a potential step of 0.03 V and a period time of 30 s. The disk rotating rate ranged from 400 to 2500 rpm. Electrochemical stability studies using cyclic voltammetry were also conducted in nitrogen-saturated 0.1 M NaOH solution at a scan rate of 50 mV/s.

Results and Discussion

XRD patterns

XRD patterns were obtained with the samples from before and after the heat treatment in the synthesis process. In the sample from before the heat treatment, the deposition of PANI-Co onto carbon support leads to the suppression of dominant carbon peaks at 25° and 44°. The well-developed crystalline structures can be assigned to the excess of the oxidant $(NH_4)_2S_2O_8$ (2θ = 17.6°, 22.2° and 26.6°). Broad polyaniline peaks located at 15.8°, 20.4° and 24.6° are also seen. After the heat treatment at 900°C in an inert nitrogen gas flowing for 1 hour, peaks resulting from the crystalline phases can be mainly assigned to Co_9S_8 (2θ = 15.3°, 29.7°, 31.2°, 39.4°, 47.5° and 51.9°) (17). Consistent with the XRD, a fitting by using a series of neighbor shells in EXAFS analysis also indicated that the preponderance of Co species in the catalyst resides in the Co_9S_8, with only a small fraction in other forms (18).

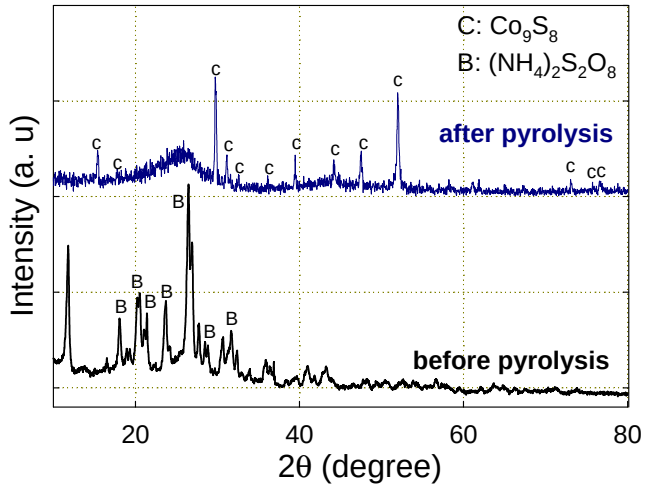

Figure 1. XRD patterns for the Co_9S_8-N-C catalyst: (a) before and (b) after a heat treatment at 900°C in an inert nitrogen atmosphere

Electron microscopy studies

SEM and TEM images for the Co_9S_8-N-C catalyst are shown in **Figures 2** and **3**, respectively. Based on the XRD pattern, the solid particles observed in SEM images are most likely Co_9S_8. Graphene-like structures are observed; they appear to surround the Co_9S_8 particles in the catalyst. The presence of graphene sheets has been clearly confirmed in HR-TEM shown in Figure 3. Interestingly, no such graphene-sheet

structures were found in similar catalysts synthesized using different nitrogen-carbon precursors (ethylene diamine, cyanamide) and transition metals such as like Fe. This significant morphological change in the PANI-Co derived catalysts implies a strong effect of the transition metal precursor on the structure of catalysts during the heat-treatment of carbon–nitrogen precursors. Co appears to be an effective catalyst for the decomposition of the polymer that may facilitate coalescence of the decomposed carbon and nitrogen species to form graphene structures during carbonization. Such highly-graphitized carbon structures in Co_9S_8-N-C may benefit the ORR electrocatalysis by, among others, assuring high electron conductivity and providing corrosion resistance.

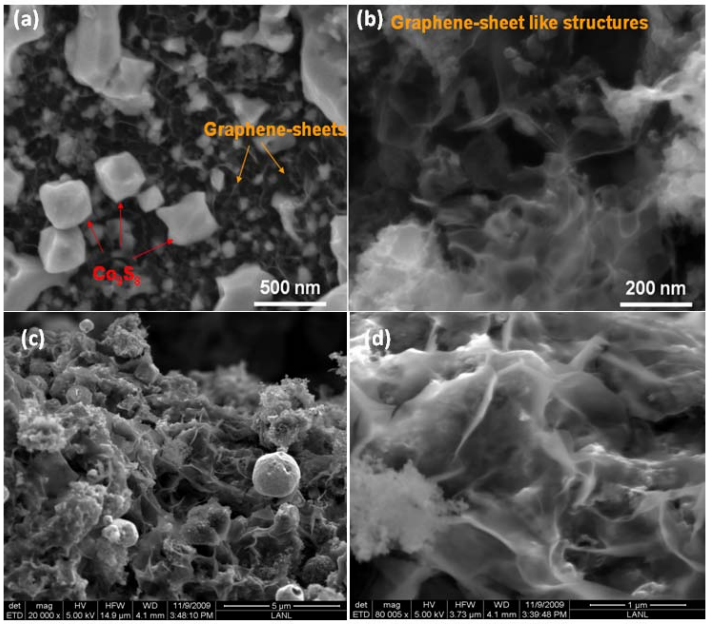

Figure 2. SEM images of Co_8S_9-N-C catalyst.

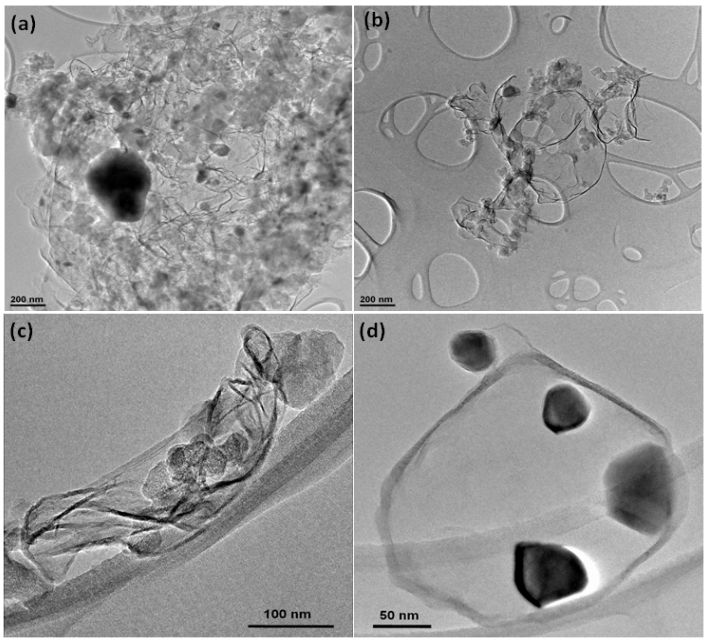

Figure 3. HR-TEM images of Co_9S_8-N-C catalyst.

XPS analysis

XPS data in **Figure 4** points to two dominant nitrogen peaks at (401.1 eV) and (398.5 eV). According to previous research (19-21), nitrogen atoms in nitrogen-doped carbon materials pyrolyzed above 700°C can be incorporated into the graphene layers and replace carbon atoms at different sites. Such processes give rise to the formation of XPS peaks reflecting differently bound nitrogen atoms: pyridinic (398.6 ± 0.3eV), pyrrolic (400.5 ± 0.3 eV), and quaternary (401.3 ± 0.3 eV). The pyridinic nitrogen represents atoms doped at the edges of the graphitic carbon layers and the quaternary nitrogen is defined as the one doped inside the graphitic carbon plane. Pyrrolic nitrogen atoms are often linked to five-member rings. Such atoms are, however, indistinguishable from pyridone (pyridinic nitrogen next to an OH group) (19). Both the pyrrolic and pyridone nitrogen atoms have been shown to decompose at temperatures above 600°C yielding pyridinic and quaternary nitrogens (19). Quaternary-nitrogen species include protonated pyridine or the "graphitic" nitrogen, in which nitrogen is within a graphite plane and bonded to three carbon atoms. Features in the high binding-energy range of the N 1s spectra (402–405 eV) can be assigned to the interaction of graphitic nitrogen with other nitrogen atoms or to the differences in the binding energy of graphitic nitrogen depending on its position in the graphite plane (19). Therefore, the two dominant peaks observed in the Co_9S_8-N-C spectrum at 398.5 and 401.1 eV (Figure 4) can be assigned to the pyridinic and quaternary nitrogens, respectively. This suggests that the N atoms were successfully incorporated into the carbon structures and replaced carbon atoms located at the edges and inside of the graphitic carbon layers. These nitrogen functionalities can be viewed in this case as *n*-type carbon dopants that lead to the formation of disordered carbon nanostructures. They donate electrons to the carbon, potentially facilitating the ORR (20).

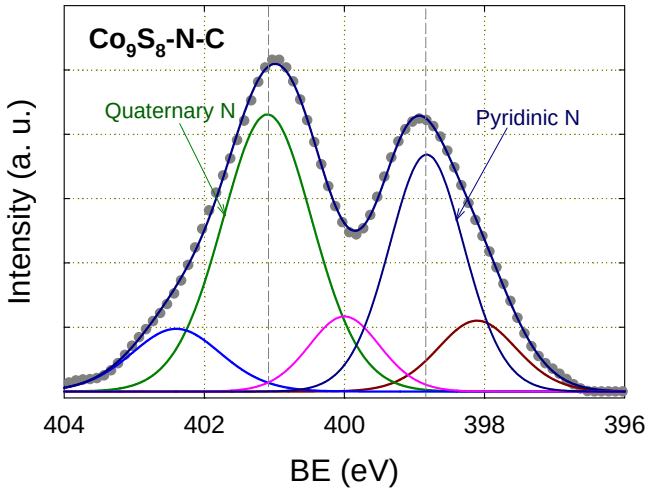

Figure 4. N 1s XPS of Co_9S_8-N-C catalyst.

ORR performance in alkaline media

The ORR on such-fabricated non-precious metal catalysts has been extensively investigated in acid media for potential application in Nafion®-based PEFCs (acid media). The ORR activity of the Co_9S_8-N-C catalyst in 0.1 M NaOH as a function of a number of potential cycles is shown in **Figure 5a**. The catalyst performance improves during the first one thousand cycles, probably due to the improved wetting of the catalyst layer or possible formation of active cobalt oxides (22). For comparison, the ORR

performance of a Fe-based non-precious metal catalyst and of a Pt reference catalyst, both of which exhibit much higher ORR activity in acid media than the Co-based catalyst (1), is shown in **Figures 5b** and **5c**, respectively. While not requiring "activation" in the initial stage of the cycling both catalysts, Pt in particular, show very good stability. The ORR performance of all three catalysts measured after 1000 potential cycles is shown in **Figure 5d**. The performance comparison attests to the superior activity of the Co_9S_8-N-C catalyst relative to Fe-N-C and Pt/C.

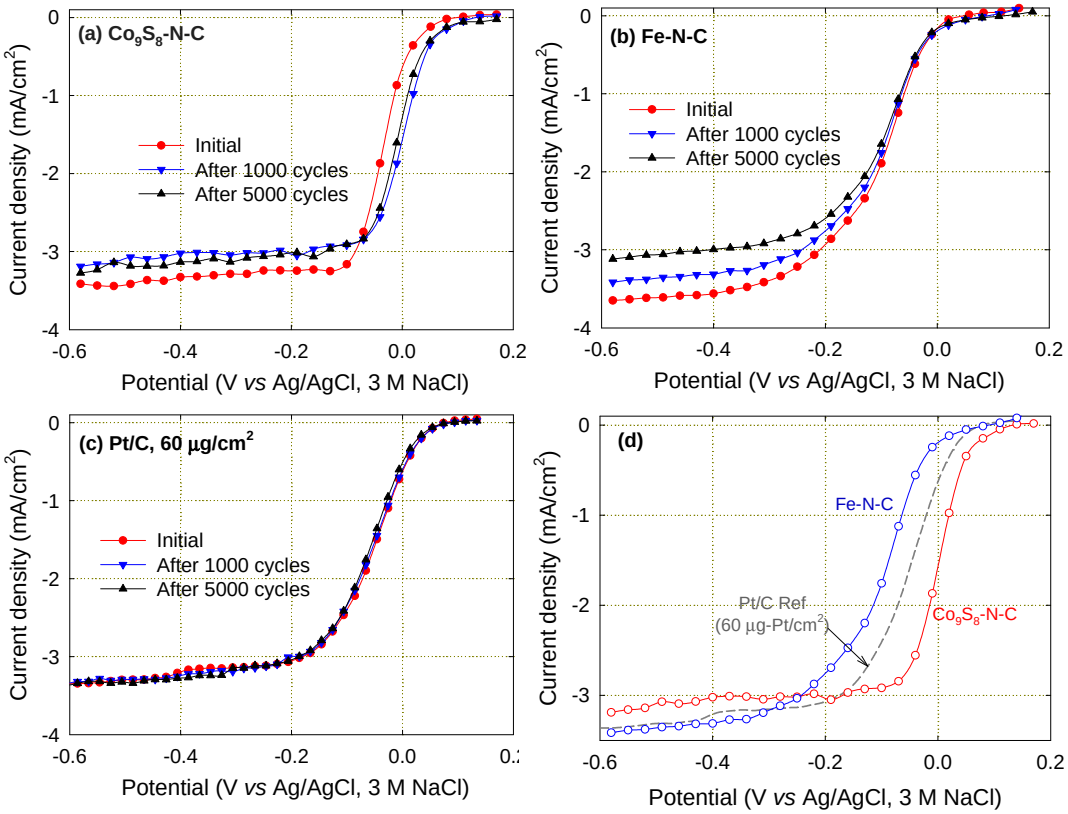

Figure 5. RDE testing of the ORR performance of (a) Co_9S_8-N-C, (b) Fe-N-C, and (c) Pt/C; (d) ORR polarization plots recorded with all three catalysts after 1000 cycles. Catalyst loading: 0.6 mg cm^{-2} for non-precious metal catalysts, 60 μg_{Pt} cm^{-2} for Pt/C; electrolyte 0.1 M NaOH; rotation rate 900 rpm; temperature 25°C. Potential cycling: range -0.6 to 0.2 V vs. 3.0 M Ag/AgCl reference; scan rate 50 mV s^{-1}; N_2-saturated 0.1 M NaOH solution.

ORR kinetic analysis

The electrocatalytic activity of the Co_9S_8-N-C catalyst was studied as a function of the disk rotation rate ranging from 400 to 2500 rpm (**Figure 6a**). A well-defined limiting current was reached at each rotation rate. The Koutecky-Levich plots at various ORR potentials for the Co_9S_8-N-C catalyst are shown in **Figure 6b**.

In the Koutecky–Levich equation for a film electrode (23, 24), the overall measured ORR current j, is related to the kinetic current j_k, and the boundary-layer diffusion-limiting current j_d. The limiting current, j_d can be expressed as:

$$j_d = 0.2nFD_O^{2/3}C_O\nu^{-1/6}\omega^{1/2} \quad (1)$$

where F is the Faraday constant, D_o is the diffusion coefficient of O_2 (1.9×10^{-5} cm^2/s), ω is electrode rotation rate in rpm, ν is kinematic viscosity of water (0.01 cm^2/s), and C_o is

the concentration of O_2 in dilute aqueous solution (1.1×10^{-6} mol/cm^3). The relationship between the measured current density and the rotation rate is given by:

$$\frac{1}{j}=\frac{1}{j_k}+\frac{1}{j_d}=\frac{1}{j_k}+\frac{1}{B\omega^{1/2}}=A+\frac{1}{B\omega^{1/2}} \quad (2)$$

where both A and *B* are constants. Based on Equations 1 and 2, the number of electrons transferred in ORR can be obtained from the slope of the 1/*j* *vs*. $1/\omega^{1/2}$ lines (25):

$$B=0.2nFD_O^{2/3}C_O\nu^{-1/6}=3.5\times10^{-5}n \quad (3)$$

The slopes of the Koutecky–Levich plots in Figure 6b, reveal *n* values between 3.6 and 3.7 in the potential range from -0.10 V to -0.52 V *vs*. Ag/AgCl. Such high *n* values indicate good four-electron selectivity of the Co_9S_8-N-C catalyst in the alkaline aqueous media via either a direct four-electron route or a "two+two" route.

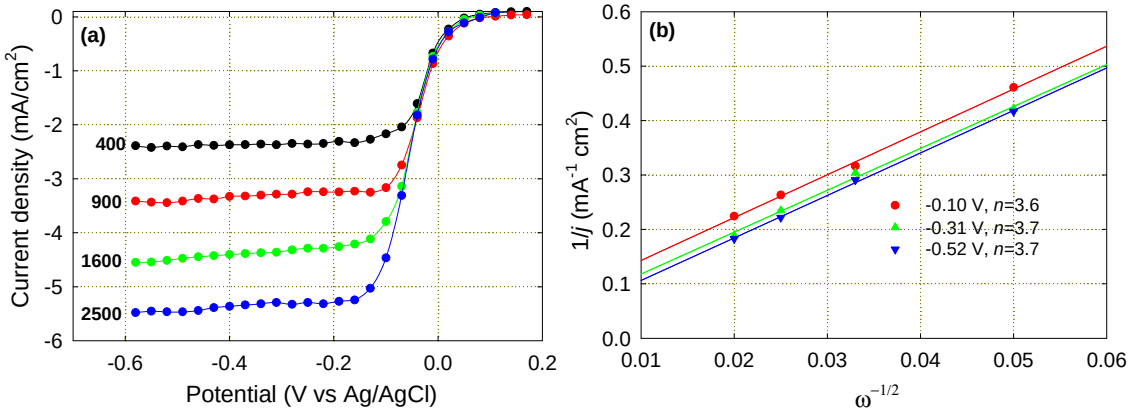

Figure 6. (a) RDE steady-state polarization curves for the ORR on the Co_9S_8-N-C catalyst in oxygen-saturated 0.1 M NaOH solution at various rotation rates (in rpm); (b) Koutecky-Levich plots for the ORR on the Co_9S_8-N-C catalyst at different electrode potentials.

Tafel slopes (*b*) were obtained to further evaluate the ORR kinetics at the Co_9S_8-N-C catalyst in alkaline media using mass transport corrected current densities. Linearly fit Tafel slopes for Co_9S_8-N-C, Fe-N-C, and Pt/C reference are shown in the **Figure 7**. The Tafel slope measured with Co_9S_8-N-C is *ca.* -63 mV/decade, while that obtained with Fe-N-C is *ca.* -80 mV/decade. This significant difference in the Tafel slope values likely indicates different ORR mechanisms and active reaction sites at the two non-precious metal catalysts.

Oxygen reduction in aqueous alkaline media is a complicated, multi-step electrocatalytic reaction. Various species have been proposed as intermediates, including O, OH, O_2^-, and HO_2^-. These species can contribute to a great number of possible reaction mechanisms (26). In this work, the Tafel slope values for ORR at the Pt/C catalyst were measured at -59 and -121 mV/decade at high and low potential, respectively. They are in a good agreement with the values reported by Damjanovic and co-workers (27). Theoretically, the Tafel slope of -118 mV/decade is due to the rate determining step associated with the first electron transfer (Langmuirian adsorption assumed). The Tafel slope of -59 mV/decade can be ascribed to the Temkin adsorption of O at a higher coverage of the surface oxide (or other oxygen intermediates), leading to a coverage-dependent activation barrier for the ORR (27, 28).

The Tafel behavior observed with Co_9S_8-N-C is quite similar to that reported for a Co-oxide electrode in the oxygen evolution reaction (OER) in alkaline media (29). The

ORR mechanism on Co_9S_8-N-C may thus be linked to the formation of cobalt oxide(s), with the reaction rate controlled by the migration of intermediates on the surface rather than the first electron transfer.

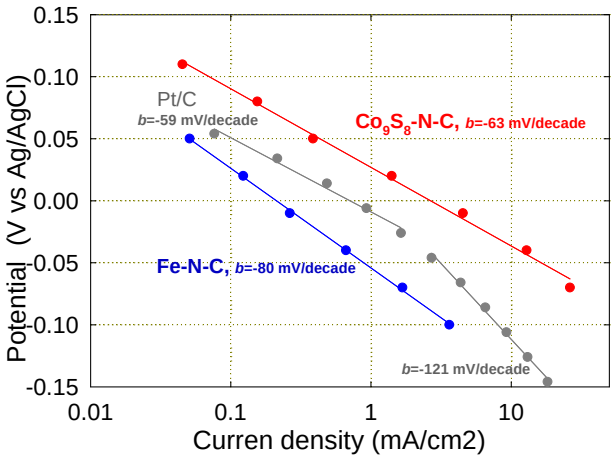

Figure 7. Mass-transport corrected ORR Tafel plots at Co_9S_8-N-C, Fe-N-C, and Pt/C in 0.1 M NaOH solution.

Conclusions

A catalyst composed of Co_9S_8 particles surrounded by nitrogen-doped graphene sheets (Co_9S_8-N-C) was synthesized for oxygen reduction in alkaline media. The catalyst shows improved ORR activity and stability relative to a Pt/C reference catalyst and a Fe-N-C non-precious metal catalyst. Oxygen can be reduced to OH^- at the Co_9S_8-N-C catalyst on a four-electron pathway. A Tafel slope of *ca.* -59 mV/decade suggests that the ORR mechanism may be controlled by an intermediate (O, OH, O_2^-, or HO_2^-) migration on the oxidized surface the catalyst. The details of the mechanism are yet unknown though, including the structure of the active ORR site(s) and the respective roles of Co_9S_8 and grapheme sheets in the reaction.

Further optimization of the Co_9S_8 content and the graphitized carbon structures as well as of the surface morphology is expected to yield even more efficient non-precious metal electrocatalysts for advanced alkaline polymer electrolyte fuel cells.

Acknowledgments

Financial support from the DOE-EERE Fuel Cells Technologies Program and the Los Alamos National Laboratory Early Career LDRD funding is gratefully acknowledged.

References

1. G. Wu, K. L. More, C. M. Johnston and P. Zelenay, *Science*, **332**, 443 (2011).
2. F. Jaouen, E. Proietti, M. Lefevre, R. Chenitz, J. P. Dodelet, G. Wu, H. T. Chung, C. M. Johnston and P. Zelenay, *Energy Environ. Sci.*, **4**, 114 (2011).
3. G. Wu, C. Dai, D. Wang, D. Li and N. Li, *J. Mater. Chem.*, **20**, 3059 (2010).

4. G. Wu, M. A. Nelson, N. H. Mack, S. Ma, P. Sekhar, F. H. Garzon and P. Zelenay, *Chem. Commun.*, **46**, 7489 (2010).
5. J. S. Spendelow and A. Wieckowski, *Phys. Chem. Chem. Phys.*, **9**, 2654 (2007).
6. N. M. Markovic and P. N. Ross, *Surf. Sci. Rep.*, **45**, 121 (2002).
7. J. L. Fernandez, D. A. Walsh and A. J. Bard, *J. Am. Chem. Soc.*, **127**, 357 (2005).
8. K. Matsuoka, Y. Iriyama, T. Abe, M. Matsuoka and Z. Ogumi, *J. Power Sources*, **150**, 27 (2005).
9. K. Scott, E. Yu, G. Vlachogiannopoulos, M. Shivare and N. Duteanu, *J. Power Sources*, **175**, 452 (2008).
10. S. F. Lu, J. Pan, A. B. Huang, L. Zhuang and J. T. Lu, *P. Natl. Acad. Sci. USA*, **105**, 20611 (2008).
11. G. G. Wang, Y. M. Weng, D. Chu, D. Xie and R. R. Chen, *J. Membr. Sci.*, **326**, 4 (2009).
12. G. Wu, G. F. Cui, D. Y. Li, P. K. Shen and N. Li, *J. Mater. Chem.*, **19**, 6581 (2009).
13. D. Baresel, W. Sarholz, P. Scharner and J. Schmitz, *Ber. Bunsen-Ges.*, **78**, 608 (1974).
14. T. Osaka, Y. Iwase, H. Kitayama and T. Ichino, *Bull. chem. Soc. Jpn*, **56**, 2106 (1983).
15. R. A. Sidik and A. B. Anderson, *J. Phys. Chem. B* **110**, 936 (2006).
16. N. P. Subramanian, X. G. Li, V. Nallathambi, S. P. Kumaraguru, H. Colon-Mercado, G. Wu, J. W. Lee and B. N. Popov, *J. Power Sources*, **188**, 38 (2009).
17. V. Rajamani and C. T. Prewitt, *Can. Mineral.*, **13**, 75 (1975).
18. G. Wu, C. M. Johnston, N. H. Mack, K. Artyushkova, M. Ferrandon, M. Nelson, J. S. Lezama-Pacheco, S. D. Conradson, K. L. More, D. J. Myers and P. Zelenay, *J. Mater. Chem.* (2011).
19. J. R. Pels, F. Kapteijn, J. A. Moulijn, Q. Zhu and K. M. Thomas, *Carbon*, **33**, 1641 (1995).
20. G. Wu, D. Y. Li, C. S. Dai, D. L. Wang and N. Li, *Langmuir*, **24**, 3566 (2008).
21. G. Wu, M. Nelson, S. Ma, H. Meng, G. Cui and P. K. Shen, *Carbon*, **49**, 3972 (2011).
22. J. R. Goldstein and A. C. C. Tseung, *J. Phys.Chem.*, **76**, 3646 (1972).
23. D. R. Lawson, L. D. Whiteley, C. R. Martin, M. N. Szentimay and J. I. Song, *J. Electrochem. Soc.*, **135**, 2247 (1988).
24. P. Wang, Z. Ma, Z. Zhao and L. Jia, *J. Electroanal. Chem.*, **611**, 87 (2007).
25. H. C. Ye and R. M. Crooks, *J. Am. Chem. Soc.*, **129**, 3627 (2007).
26. J. L. Valdes and H. Y. Cheh, *J. Electrochem. Soc.*, **132**, 2635 (1985).
27. D. B. Sepa, M. V. Vojnovic and A. Damjanovic, *Electrochim. Acta*, **25**, 1491 (1980).
28. K. Tammeveski, M. Arulepp, T. Tenno, C. Ferrater and J. Claret, *Electrochim. Acta*, **42**, 2961 (1997).
29. G. Wu, N. Li, D. R. Zhou, K. Mitsuo and B. Q. Xu, *J. Solid State Chem.*, **177**, 3682 (2004).